JoT JOURNAL OF TURBULENCE

http://jot.iop.org/

Large-eddy simulation of turbulent wavy boundary flow—illustration of vortex dynamics*

Yu-Heng Tseng[1] **and Joel H Ferziger**

Environmental Fluid Mechanics Laboratory, Stanford University, Stanford, CA 94305-4020, USA
E-mail: yhtseng@pegasus.me.jhu.edu

Received 16 November 2003
Published 7 September 2004
doi:10.1088/1468-5248/5/1/034

Abstract. Large-eddy simulation (LES) is used to investigate three-dimensional turbulent flow over a wavy boundary. An efficient immersed boundary method (IBM) for simulating turbulent flows in complex geometries is presented. The method is based on a finite-volume approach on a non-staggered Cartesian mesh and a fractional-step method. A force is applied on the body surface through an immersed ghost-cell method. Both steady and unsteady flows are simulated. A steady flow simulation provides not only the mean and turbulence statistics but also visualization of the Görtler vortices. The simulation shows that Görtler vortices are formed by a sequential vortex reconnection process and broken down due to vortex separation. The unsteady oscillatory flow displays the three-dimensional vortex formation/transport cycle which is shown to be important for sediment transport. The turbulent structure is fully three-dimensional and is clearly seen from the current animations.

PACS numbers: 47.32Cc, 47.27.Eq

JoT 5 (2004) 034

* This paper was chosen from Selected Proceedings of the Third International Symposium on Turbulence and Shear Flow Phenomena (Sendai, Japan, 24–27 June 2003) ed N Kasagi *et al.*

[1] Present address: Department of Mechanical Engineering, Johns Hopkins University, Baltimore, MD 21218, USA.

 PII: S1468-5248(04)72047-0 1468-5248/04/000001+23$30.00

Contents

1. Introduction

Three-dimensional turbulent flows over a wavy boundary are interesting because the geometrical configuration is fairly simple but the flow pattern is complicated. The flows are subject to the effects of alternating convex and concave curvature. Many laboratory experiments, including steady flow (see e.g. [1, 2]) and unsteady oscillatory flow (see e.g. [3, 4]) were presented in the past. In steady flows, it was found that a wavy surface substantially modifies flat-wall turbulence results such as the law of the wall and turbulence production mechanism for medium-amplitude wavy surface [1]. The presence of recirculating flow caused large fluctuations of the shear stress and of the pressure near the wavy wall. However, most of the experimental studies were either limited to two dimensions or a synthesis of data measured at several discrete locations. Using large-eddy simulation (LES), Calhoun and Street [5] identified the occurrence of Görtler vortices in the turbulent flow over wavy boundary. Görtler vortices are streamwise-oriented coherent structures that often occur in counter-rotating pairs. Saric [6] provided an extensive review of Görtler instability and vortices. Most previous experimental and theoretical studies of Görtler vortices focused mainly on linear stability analysis and early transition from laminar to turbulent flows. Development of the three-dimensional structures of the Görtler vortices and the interaction of vortex pairs are still not clear due to the complexity of the non-linear system [6, 7]. Furthermore, the spatial evolution of the Görtler vortex involves not only a single instability mechanism, but also a secondary instability, initial condition, local topography effects and open convective flow, etc. These interactions cannot be addressed correctly by the local analysis and linear stability theory. Saric and Benmalek [8] showed that convex curvature has an extraordinary stabilizing influence on the Görtler vortex. The nature

of stabilization in the convex portion of the wavy wall often overcomes the destabilization of the concave region. The formation mechanism of the Görtler vortices depends significantly on the stabilization/destabilization effects of the convex/concave portion of the wavy surface. Computational methods provide a tool to identify and further investigate the vortex structures that persist in the turbulent flows over a wavy boundary.

On the other hand, the primary issues in computational fluid dynamics are accuracy, computational efficiency and, especially, the handling of complex geometry. There are many methods for solving incompressible flow in geometrically complex regions. A grid that is not well-suited to the problem can lead to numerical instability. Techniques that are often employed to handle geometry other than rectangular geometry are coordinate transformation and boundary-fitted grids [9]. These methods have the obvious advantage that the grid conforms to the irregular boundary, which is especially important when thin boundary layers are present. The disadvantage of these methods is that transformations are possible only for a limited range of geometries. To handle more complicated geometries, such as multiply connected domains and irregular objects, one must resort to more complex transformations, a task that is quite challenging. In some applications, finite element methods (FEM) on unstructured meshes are used almost exclusively. Since discrete spatial elements are aligned with the irregular boundary, important boundary effects can be well resolved. Moreover, an unstructured finite element mesh can be easily refined where details of the solution need to be resolved. The accuracy of the finite element method can be improved by using higher-order interpolation schemes, and spectral accuracy can be achieved. However, generating the meshes required by the FEM is as much an art as science and higher-order methods on an unstructured grid are expensive and difficult. Furthermore, to solve problems with a moving boundary, one must remesh every time the boundary moves, which can be very expensive.

The development of accurate and efficient methods that can deal with arbitrarily complex geometry would represent a significant advance. The immersed boundary method (IBM) has recently been demonstrated to be applicable to complex geometries while requiring significantly less computation than competing methods without loss of accuracy [10, 11]. The method specifies a body force in a way that simulates the presence of a body. The main advantages of the IBM are memory and CPU savings and ease of grid generation compared to unstructured grid methods [11], while the boundary varies with time. Bodies of almost arbitrary shape can be dealt with by additional local refinement. The local refinement on a Cartesian grid is easily achieved [12]. Furthermore, flows with multiple bodies or islands may be computed at reasonable computational cost. The IBM has been applied to various problems of irregular geometry, see [13, 14] for a recent review.

In this paper, we extend the IBM through a ghost-cell method to LES of three-dimensional turbulent flow over a wavy boundary. The systematic treatment of various boundary conditions and validation are described in [13]. The purpose of this paper is to illustrate the flexibility of the IBM and investigate the vortex structure in the turbulent flow over a wavy boundary. Both steady and unsteady flows are simulated. The steady flow simulation provides not only the mean and turbulence statistics but also visualization of the Görtler vortices formation/destruction processes. The unsteady oscillatory flow displays the three-dimensional vortex formation/transport cycle which is shown to be important for erosion and sediment transport in environmental flows [15, 16].

This paper is organized as follows. Section 2 introduces the governing equations and numerical implementation of the method. Section 3 presents the LES results of three-dimensional turbulent flow over wavy boundary using a Cartesian grid and investigates the formation/destruction of Görtler vortices. Finally, conclusions are drawn in section 4.

2. Numerical method and model description

2.1. Governing equations

In order to model the flows of interest, we consider the three-dimensional, unsteady, incompressible Navier–Stoke equations in Boussinesq form and the continuity equation. When writing these governing equations in conservative form, we obtain

$$\frac{\partial u_j}{\partial x_j} = 0, \tag{1}$$

$$\frac{\partial u_i}{\partial t} + \frac{\partial}{\partial x_j}\left(u_i u_j + p\delta_{ij} - \nu\frac{\partial u_i}{\partial x_j}\right) = F_i, \tag{2}$$

where p is the pressure and $\nu = \mu/\rho_0$ is the kinematic viscosity. F_i is the additional forcing and is zero everywhere except at the immersed boundary. The Einstein convention is used to imply summation over repeated indices.

2.2. Filtered governing equations

In LES, each flow variable f is decomposed into a large-scale (or resolved) component $\overline{f}$ and a subfilter-scale (or unresolved) component f'

$$f = \overline{f} + f'. \tag{3}$$

Following the work of Zang [17], the governing equations are filtered so that they solve for the resolved motion. The filtered equations for equations (1) and (2) become

$$\frac{\partial \overline{u}_j}{\partial x_j} = 0, \tag{4}$$

$$\frac{\partial \overline{u}_i}{\partial t} + \frac{\partial}{\partial x_j}\left(\overline{u}_i\overline{u}_j + \overline{p}\delta_{ij} - \nu\frac{\partial \overline{u}_i}{\partial \overline{x}_j}\right) = \overline{F}_i - \frac{\partial \tau_{ij}}{\partial x_j}. \tag{5}$$

These equations govern the evolution of the large, energy-carrying, scales of motions. An extra term which represents the effect of the unresolved, or subfilter-scale, on the resolved part of turbulence also appears in the above equations. The term is the subfilter-scale (SFS) stress tensor τ_{ij}, defined as

$$\tau_{ij} = \overline{u_i u}_j - \overline{u}_i\overline{u}_j. \tag{6}$$

Here, we use a dynamic subfilter scale model with local averaging for computing the influence of these small scales [18, 19]. This model predicts the correct asymptotic behaviour near the boundaries and allows energy backscatter and it is used successfully for many flows.

2.3. Numerical formulation

The governing equations (4) and (5) are solved using a finite-volume technique. The method of fractional steps (a variant of the projection method), which splits the numerical operators and enforces continuity [20] by solving a pressure Poisson equation, is adopted. The diagonal viscous terms in equation (5) are discretized with a Crank–Nicholson scheme and all other terms are treated explicitly with the second-order Adams–Bashforth scheme. All spatial derivatives are discretized using second-order central differences with the exception of the convective term.

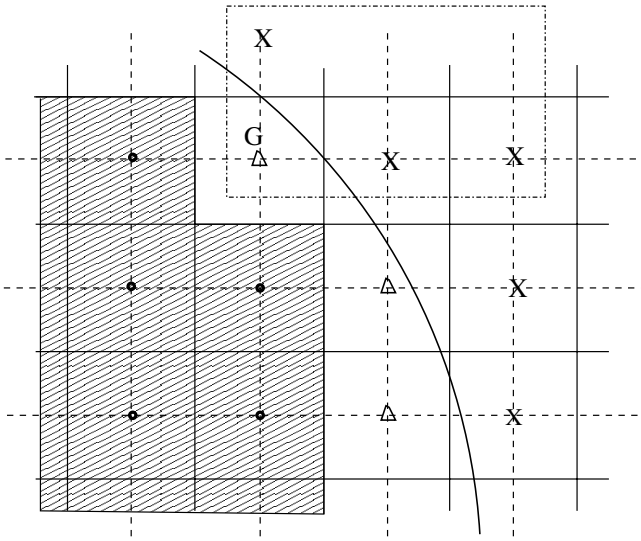

Figure 1. Schematic of the computational domain with an immersed boundary. ×, point in the physical domain; △, the ghost-cell domain.

That term is discretized using QUICK [21] in which the velocity components on the cell faces are computed from the nodal values using a quadratic interpolation scheme. Further details of the method can be found in [9, 22]. The original three-dimensional pressure Poisson equation is solved by a multi-grid (MG) method. In the current study, a strongly implicit procedure (SIP) preconditioned bi-conjugate gradient stabilized (Bi-CGSTAB) iterative method is used to solve the pressure Poisson equation. This method has been shown to accelerate the convergence significantly [13].

2.4. Ghost-cell method for an immersed boundary

The systematic treatment of various boundary conditions is detailed in [13]. We develop an alternative approach through the use of a ghost zone. In order to represent the complex boundary on a Cartesian grid, a boundary forcing term F_i is added to the momentum equation implicitly through ghost cells [13]. The present approach is more flexible with respect to the incorporation of boundary conditions. The force F_i is correct for the case in which the position of the unknowns on the grid coincides with the immersed boundary; this requires the boundary to lie on coordinate lines or surfaces, which is not possible for complex geometries. Many different techniques have been adopted and they can be classified into two groups: (a) schemes that spread the forcing function over the vicinity of the immersed surface, and (b) schemes that produce a local reconstruction of the solution based on the boundary values [14]. In fact, the two approaches are equivalent. The original Peskin [23] method, which substitutes a discrete Dirac δ function in equation (5), belongs to the first category. The local reconstruction scheme (b) has been proved to be more flexible [10, 11, 24] and can be designed so that it has a high degree of accuracy. The current ghost-cell method belongs to the second category. The immersed boundary and a ghost-cell zone are illustrated in figure 1. We express the flow variables in terms of a polynomial and use it to evaluate the ghost point values. We use linear and quadratic approaches which preserve the second-order accuracy of the overall numerical scheme [13]. The scheme is equally applicable to steady and moving boundaries. A detailed description of the numerical procedure can be found in [13].

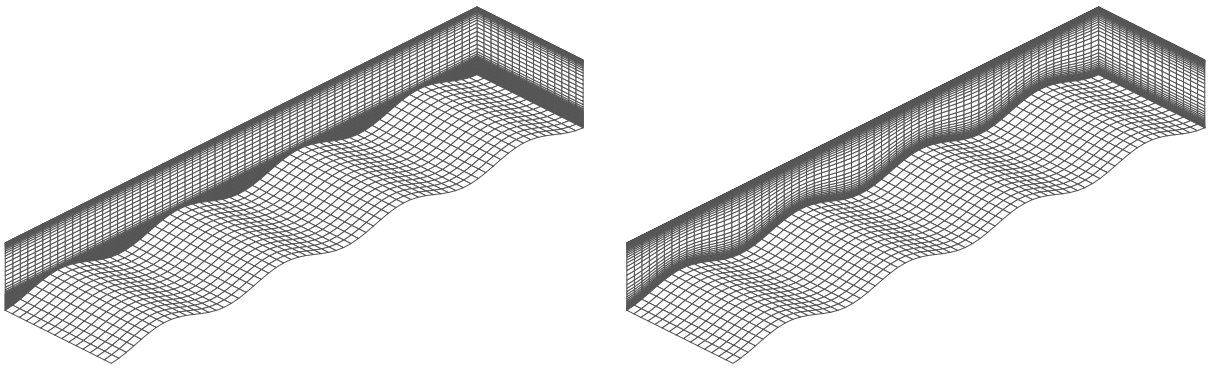

(a) (b)

Figure 2. Comparison of the computational domains between the IBM (a) and boundary-fitted (b) grids for the wavy channel flow; the domain size is 20.3 cm × 4.8 cm × 2.1 cm. The bottom wavy boundary in (a) is derived from the boundary-fitted grid (every second grid point in each direction is shown).

It is important to note that for the forcing of Saiki and Biringen [25] and Goldstein *et al* [26], the velocity at the immersed boundaries was imposed by a fictitious force. In the current approach, the boundary condition is imposed directly. This implies that, in contrast to the feedback forcing method, the stability limit of the current integration scheme is the same as that without the immersed boundaries, thus making simulation of complex three-dimensional flows practical. Higher-order extrapolation/interpolation schemes to evaluate the variables at the ghost cells can preserve at least second-order spatial accuracy [27, 28].

In LES, the value of the turbulent viscosity ν_T at all fluid points, including the ghost points shown in figure 1, is required to compute the diffusive fluxes. The computation of ν_T at the force points is not straightforward in [10, 24] since the evaluation of all test-filtered quantities would include points in the interior of the solid body. Using the ghost points inside the boundary avoids possible errors and imposes an approximation of the proper value. For the LES that has been carried out in this study, the error in the turbulent viscosity is found to be small, mostly because of the fine grids required to resolve the thin bottom boundary layers around immersed bodies. For coarser grid or atmosphere boundary layer, alternative reconstructions can be considered.

2.5. Description of the simulations

Large-eddy simulation is employed to simulate flow over a wavy boundary. The IBM described in section 2.4 is applied and compared with the results of Zedler and Street [29]. The second-order overall accuracy of the IBM has been validated in Tseng and Ferziger [13]. Zedler and Street [29] used a non-orthogonal, boundary-fitted grid to compute turbulent flow over a wavy boundary and study sediment transport in the flow. Their results have been compared with laboratory experiments for the same geometry [5]. The calculations are three dimensional and both steady and unsteady flows are simulated.

The bottom boundary configures straight-crested transverse ripples $A\sin(2\pi x/\lambda)$, where A = 0.254 cm is the ripple amplitude; and λ = 5.08 cm is the ripple wavelength. The domain is roughly the same with dimensions of 20.3 cm × 4.8 cm × 2.1 cm ($L \times W \times H$) as shown in figure 2 for the IBM and boundary-fitted grids. A grid of 130 × 34 × 130 is used in the IBM simulation while a grid of 130 × 34 × 98 is used in the boundary-fitted grid case. Both grid configurations employ exponential stretching vertically. A grid size 1.5 times larger is used in

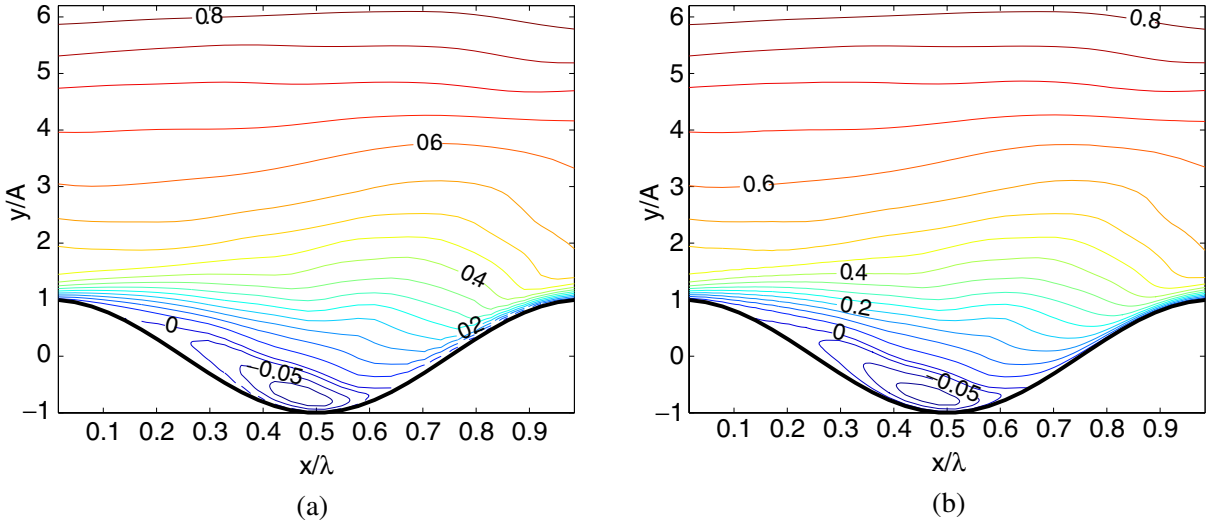

Figure 3. Comparisons of streamwise velocity profile from the (a) IBM and (b) boundary-fitted grid results for steady flow.

the vertical direction for the IBM case to ensure the first few grids above the wave crest to have similar grid density as that in the boundary-fitted grid case. Grid resolution study for this flow configuration has been tested in previous studies [15, 29, 30], showing that the current configuration can accurately describe the turbulent flow over a wavy boundary. The steady flow is driven by a uniform pressure gradient that yields a Reynolds number of about 2400, based on a channel height of 2.1 cm and the mean streamwise velocity. The unsteady flow is driven by an oscillatory pressure gradient (a simple sinusoidal function) that yields the same Reynolds number based on the maximum velocity. The boundary conditions are periodic on all lateral boundaries, free-slip (zero stress) at the top and no-slip at the wavy bottom. A detailed description of this type of flow can be found in [15, 29].

3. Simulation results

3.1. Steady-flow simulations

The steady-flow configuration has been studied extensively in the past [5, 31, 32]. The flow pattern is characterized by strong streamwise vortices, which begin on the upslope portion of the wave and end before the next crest. For moderate slopes, the flow separates just downstream of the crest and an unsteady recirculation zone appears. In the reattachment region, usually just downstream of the trough, a thin accelerating boundary layer forms due to the decreasing cross-section and lifts away from the surface forming a detached shear layer as it moves over the crest. The flow can be divided into four regimes: an outer flow, a separated region, an attached boundary layer on the upslope side of the wavy boundary, and a free shear layer which is located in the lee side of the crest and is characterized by a large velocity gradient. Thus, an accurate representation of the detailed dynamics of this flow is a challenging task for Cartesian grids.

3.1.1. Comparison with boundary-fitted grid results. For purposes of comparing with boundary-fitted grid results, the contours of mean streamwise velocity in one wavelength of the topography are shown. The mean streamwise velocities are compared in figures 3(a) and (b), respectively.

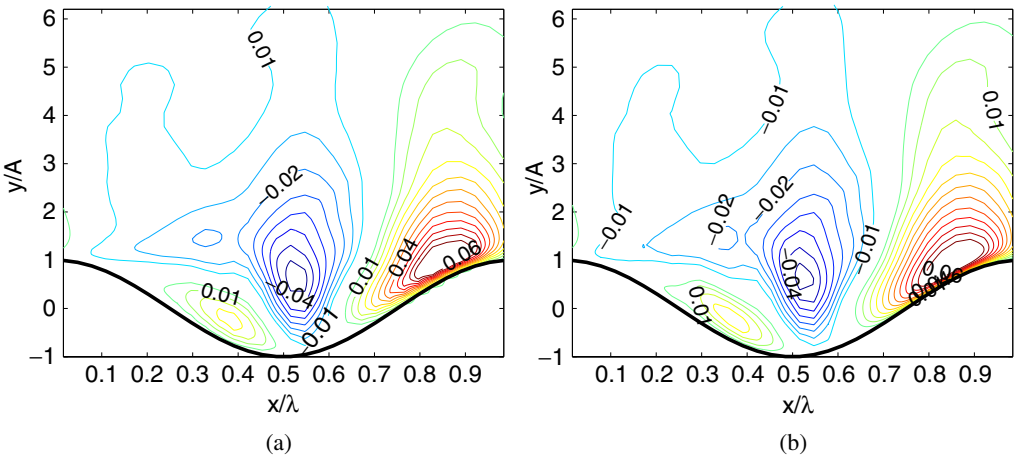

Figure 4. Comparisons of mean vertical velocity contours between the (a) IBM and (b) boundary-fitted grid results for steady flow over one wavelength of the topography. The boundary-fitted grid result is much smoother in the up-slope region since more grid points are used.

The contours are normalized by the maximum streamwise velocity at the top (u_t). The differences between the IBM and boundary-fitted profiles for the mean streamwise velocities are very small. In particular, the profiles in the outer regions (beyond $(y - y_0) = 0.3h$, y_0 being the height of bottom topography) identified by Calhoun and Street [5] are almost identical. The differences between the average velocity profiles over the crest are small, which shows that the wavy wall behaves as an equivalent roughness in both cases. The separation flow is characterized by the presence of a recirculation zone developed downstream of the wave crest.

The contours of mean vertical velocity (v/u_t) from the IBM and boundary-fitted grid results are compared in figure 4. The agreement is very good. The vertical velocity is more sensitive to the method than the streamwise velocity since its magnitude is much smaller ($O(10^{-2})$). The recirculation is apparent in the mean vertical velocity contour as positive vertical velocities on the downward sloping portion of the surface. The vertical velocity contours obtained with the IBM are very similar to the contours produced by the boundary-fitted grid.

The spatial distribution of pressure on the bottom boundary between the IBM and boundary-fitted grid results is compared in figure 5. Accurate prediction of pressure is clearly an important aspect to evaluate the boundary behaviour of the IBM. The pressure distribution is very sensitive to the boundary treatment and varies with the slope, wavy shape and Reynolds numbers. The global averaged pressure P_0 is subtracted out. In the present study, all quantities (e.g. velocity, pressure, shear stress, etc) are linearly interpolated from the nearest cells. Both simulations show very similar pressure distribution on the bottom boundary surface. The spatial distribution of the pressure is negative along the downslope portion on the bottom surface and reaches its minimum in the vicinity of the wave crest. Positive pressure is observed in the upslope portion of the wave crest. In the troughs the pressure is almost zero. These features are also observed in previous numerical and laboratory experiments for turbulent flow over wavy boundary [2, 32]. Quantitative comparison of spanwise-averaged pressure along the bottom boundary in one wavelength of the topography is shown in figure 6. It is clear that both IBM and boundary-fitted grid results predict the pressure increase on the upslope portion quite well. The magnitude of the pressure is slightly different in the vicinity of wave trough. Overall, the results show that the pressure on the bottom surface is well predicted using the IBM.

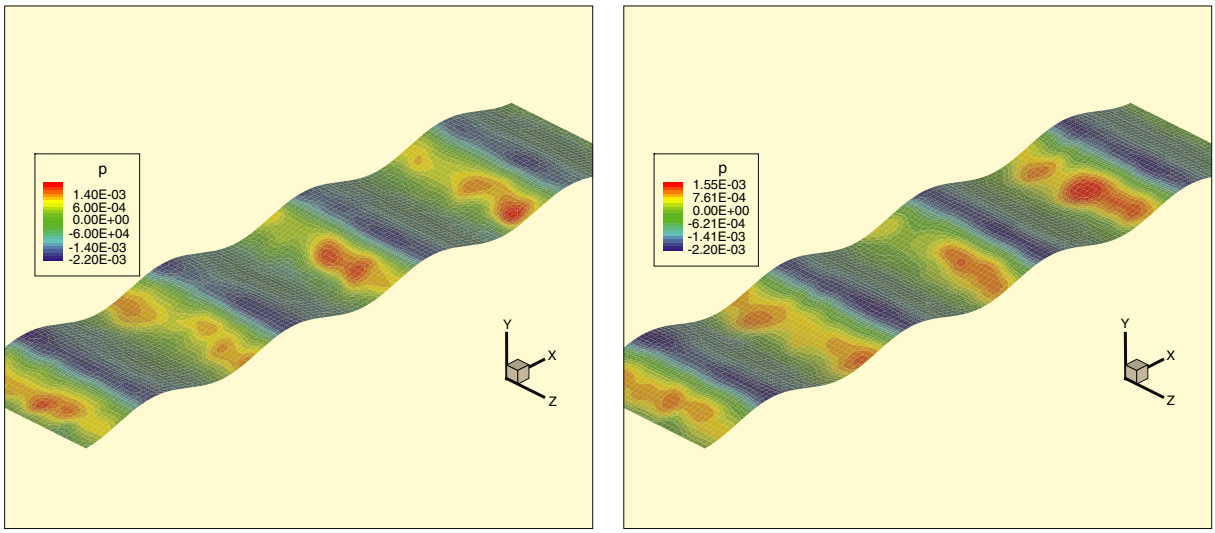

(a) (b)

Figure 5. Comparisons of the bottom pressure contours between the (a) IBM and (b) boundary-fitted grid results for steady flow. The global averaged pressure is subtracted out.

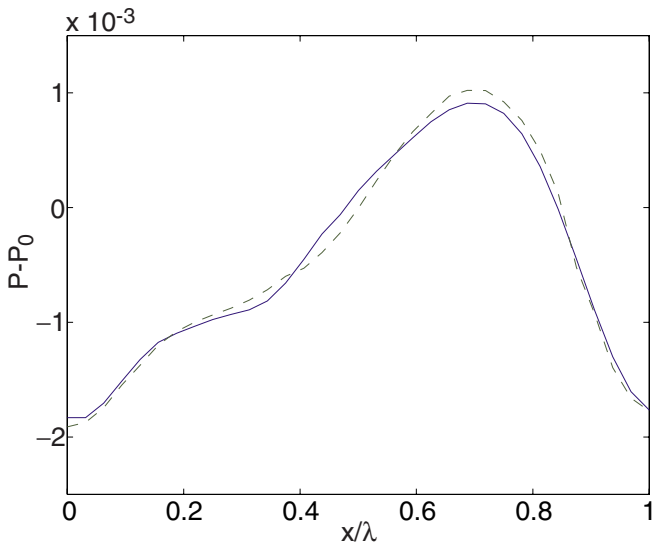

Figure 6. The spanwise-averaged pressure on the bottom surface for steady flow. —, boundary-fitted grid results; – –, IBM results.

Note that we did not perform a comparison for the computational time. The current IBM is directly implemented on the same code used in the boundary-fitted grid case. The computational grid is reconstructed to generate its orthogonal mesh. The main purpose of this study is to illustrate the flexibility of the IBM (handling complex geometry accurately) and the ease of implementation in any existing code. All metric terms and coordinate transformations are not removed in this study although they are redundant for the IBM grid. On an orthogonal grid,

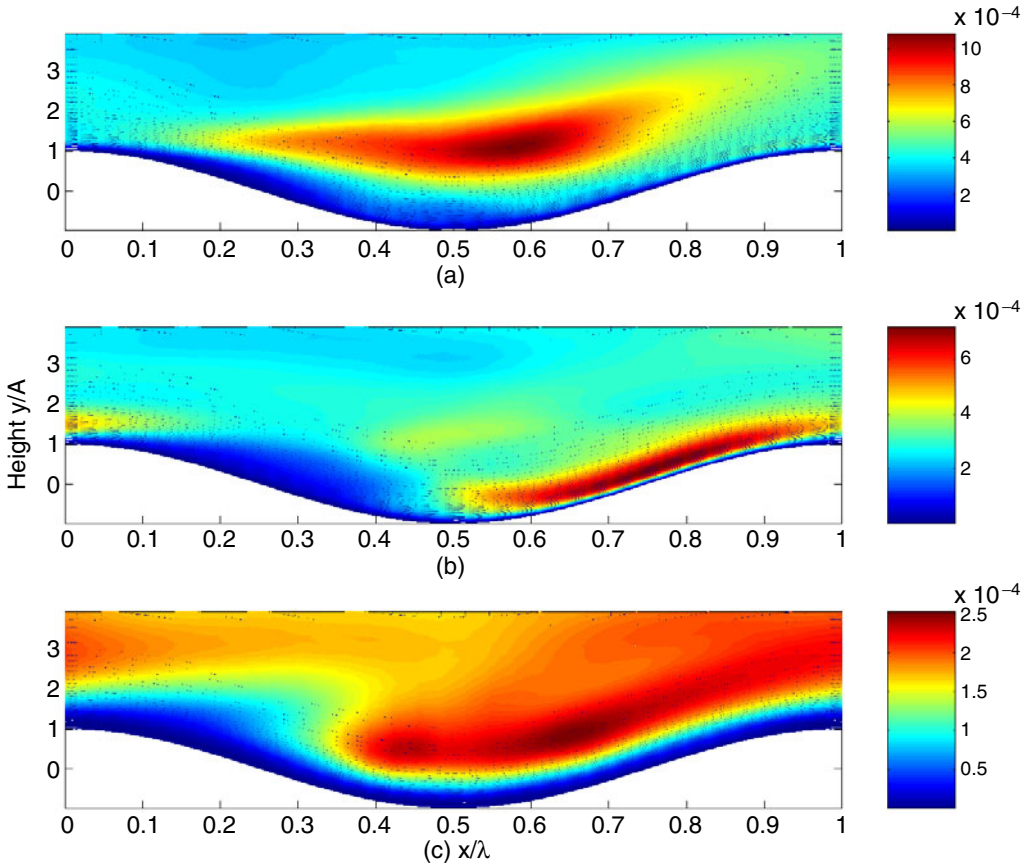

Figure 7. Colour contours of mean flow turbulence intensity: (a) streamwise turbulence intensity $\overline{u'^2}$, (b) spanwise turbulence intensity $\overline{w'^2}$ and (c) vertical turbulence intensity $\overline{v'^2}$.

accurate representation for this flow is more important. In addition, this code will be optimized to simulate moving wavy ripples in future work. Significant saving on the CPU time will be achieved since no grid remeshing is needed and all redundant variables and transformations will be removed.

3.1.2. Turbulent quantities and bottom shear stress. Strengths of the components of turbulence intensity (TI) are shown in figure 7. The maximum streamwise $\overline{u'^2}$ is found above the centre of the trough and is associated with the shear layer that detaches from the surface at the separation point. Contours of the vertical TI show that the maxima locates slightly downstream of the location of the maximum streamwise TI. The maximum value is about one third of the streamwise value. Henn and Sykes [32] noted an increase in spanwise velocity fluctuations on the upstream slopes of their wavy boundary and suggested that the precise mechanism responsible is not yet known. Calhoun and Street [5] concluded that Görtler instability appears to be important in the formation of the vortices and associated with the increase in spanwise velocity fluctuation. As shown in figure 7(b), the spanwise TI shows a marked increase on the upslope close to the wavy surface. The magnitude and location suggest a localized production mechanism associated with the waviness of the boundary. These features confirm

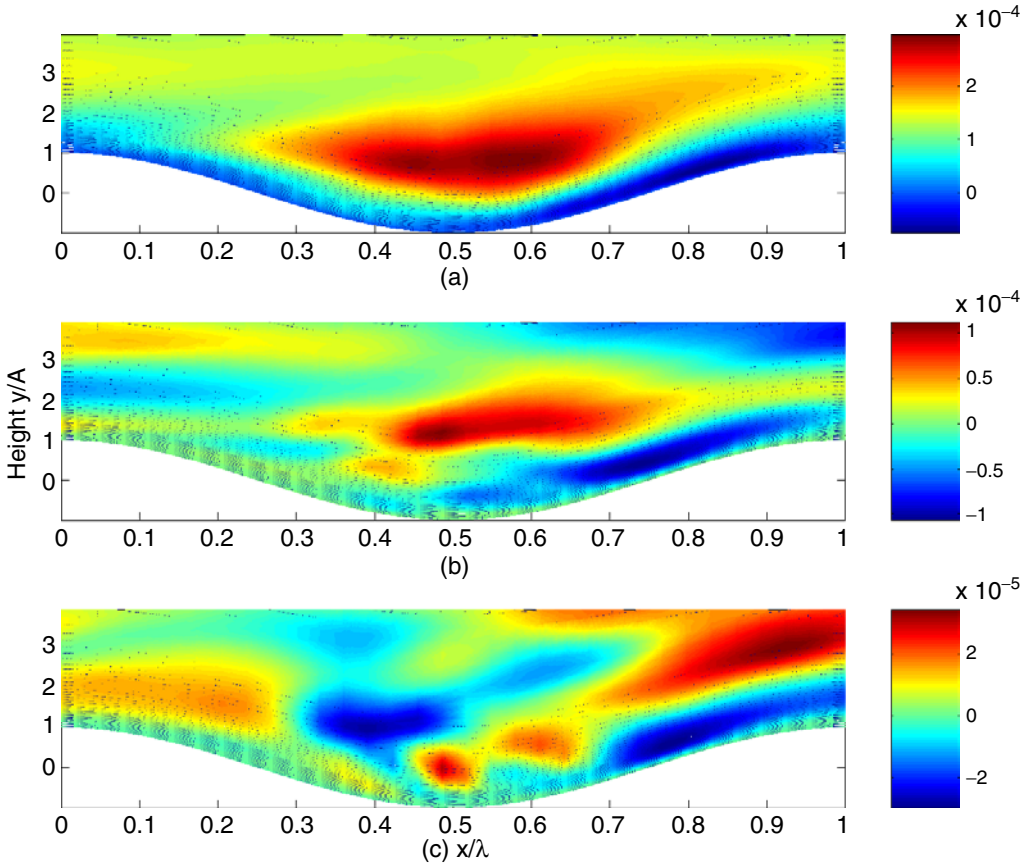

Figure 8. Colour contours of mean turbulent Reynolds stress in one wavelength of the topography for (a) Reynolds stress $-\overline{u'v'}$, (b) Reynolds stress $-\overline{u'w'}$ and (c) Reynolds stress $-\overline{v'w'}$.

the link between the streamwise vortices and the increase of spanwise TI found by Calhoun and Street [5].

The turbulent Reynolds stresses in one wavelength of the topography are shown in figure 8. The maximum turbulent fluctuation $-\overline{u'v'}$ and $-\overline{u'w'}$ is located above the trough and is associated with the separated shear layer. The maximum magnitude of the turbulent fluctuation $-\overline{v'w'}$ is much smaller than the other components of turbulent Reynolds stresses. A region with small negative values of Reynolds stress exists close to the upslope surface and is an artifact of the Cartesian coordinate used [5]. These values become positive while it is rotated into a boundary-layer coordinate system.

Figure 9 shows the spatial distribution of the magnitude of the bottom boundary shear stress. The magnitude of shear stress increases in the upslope portion of the wave crest. The distribution is not uniform across the spanwise direction. The increase just ahead of the wave crest is of larger magnitude than that just above the trough. The increase of shear stress is mainly associated with the turbulent intensity increase as described above in that region.

3.1.3. Three-dimensional structure of Görtler vortices. In order to further investigate the structure of the vortex cores, we have generated the contour animation of the second invariant (λ_2) of the velocity gradient tensor [33] in animation I. This approach is a variant of the pressure

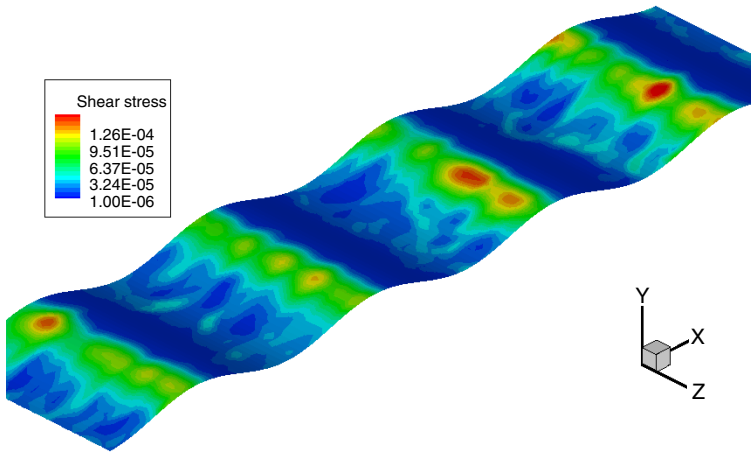

Figure 9. The time-averaged shear stress contours on the bottom surface for steady flow.

minimum method. The presence of these vortices is indicative of active regions of the flow. The vortex cores resemble those in channel flow, but they are longer, taller and have a greater angle of inclination [5]. These vortices intensify and grow over the crest and then lose their identity over the trough, resulting from the Görtler instability associated with boundary curvature [5, 8, 29].

The Görtler instability occurs as the shear flow over a concave surface is subject to a centrifugal instability. The Görtler instability and secondary instability due to the distortion of the mean velocity field may cause transition to turbulence. However, the development process is still not clear due to its complexity and nonlinearity. The formation mechanism of the Görtler vortices depends significantly on the stabilization/destabilization effects of the convex/concave portion of the wavy surface [8]. In this section, we use the λ_2 method to explore the formation, evolution and breakdown processes of Görtler vortices.

When the vortices move across the trough, passing over the inflection point, the Görtler vortex begins to form and strengthen through the vortex reconnection process [34]. Figure 10 is taken from the the animation of $\lambda_2 = -150$ (animation I) and shows the formation of such a process over the concave surface. When convecting over the trough, the vortices B_1 and B_2 are very sensitive to any instability mechanism. These vortices tend to develop slight kinks. The velocity induced by the kinks tends to stretch and lengthen them further. The variations in the separation and strength of the vortices cause interactions among these two vortices (B_1 and B_2) and agglomerates them to produce a single larger vortex (figures 10(b) and (c)). This pairing process results in a reconnection process [35]. The vortices B_1 and B_2 connect and then become a larger vortex B_1 in figure 10(c). It appears that the pairing intensifies the vortex strength. Furthermore, the stretching of the kink induces the neighbouring vortex B_3 to kink, producing a kind of chain reaction (figure 10(d)). When these vortices move further downstream over the concave trough, the reconnecting process is repeated and vortex B_3 merges with vortex B_1, thus producing a even larger vortex which tilts when passing over the trough (figure 11). These processes are supported by the simulation results of Saric and Benmalek [8]. They provided examples which added an oppositely rotating vortex pair in the convex region and their results showed significantly stabilizing effects and hence the flow is unlikely to be subjected to Görtler instability.

A typical Görtler vortex (B_1) is then clearly seen growing in figures 11(a)–(d) while it moves further downstream over the upslope portion of the second wave crest. Calhoun and

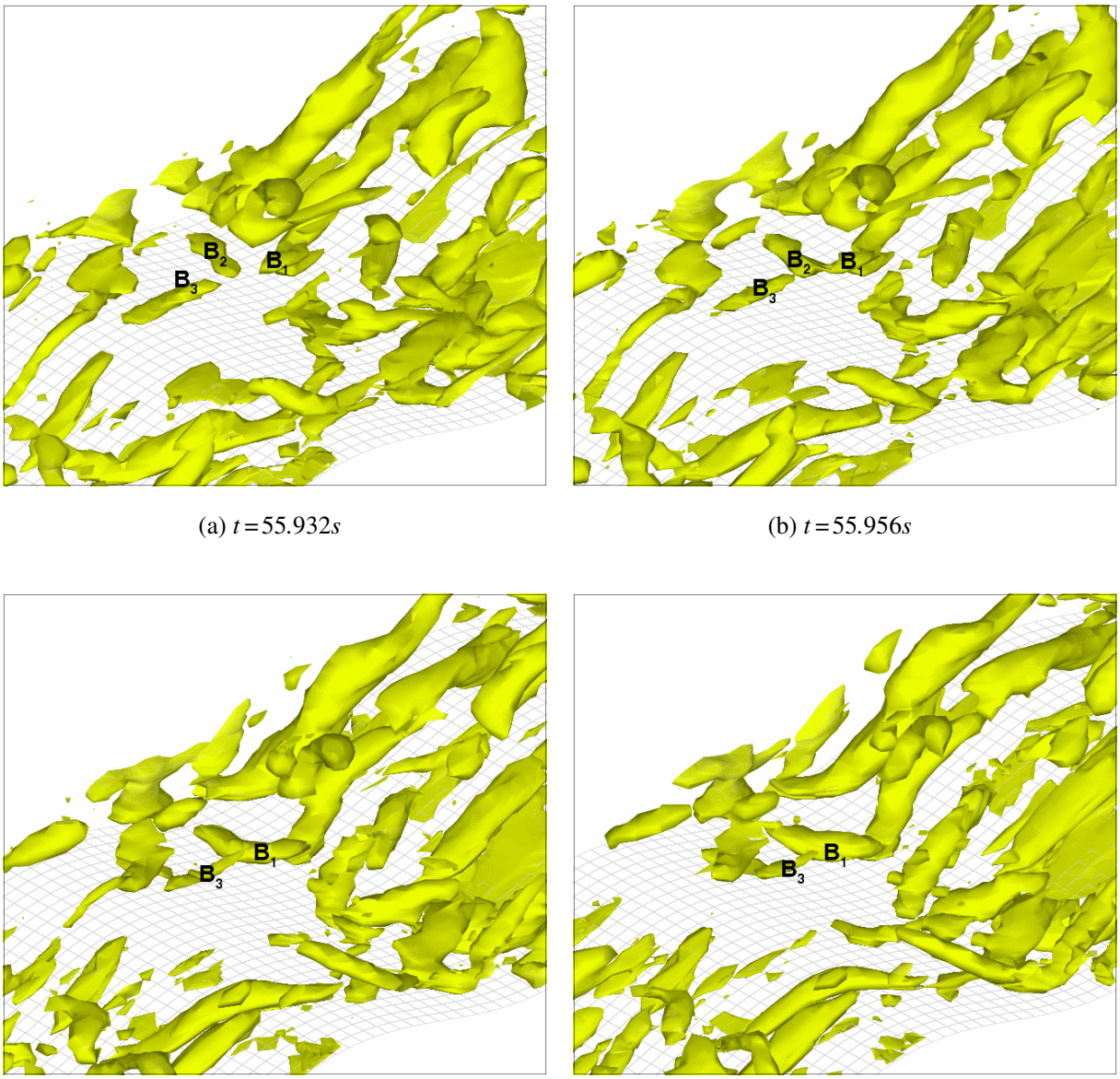

(a) $t = 55.932s$ (b) $t = 55.956s$

(c) $t = 55.980s$ (d) $t = 56.004s$

Figure 10. Time-evolved vortex structures plotted with the λ_2 method in fully developed steady wavy flow (isocontours of $\lambda_2 = -150$). (See animation I.)

Street [5] computed the Görtler number ($G = (\kappa\lambda)^2/(v/u\lambda)$, where κ is the curvature of the local streamline) and determined that the inception of the vortex cores occurred at the upslope portion of the wave crest. It is the ratio between the inertial and centrifugal effects to the viscous effects. Regions in the flow characterized by large positive values of the Görtler number are susceptible to the Görtler instability. These results are consistent with the increase of spanwise turbulence intensity in figure 7.

Figures 12(a)–(d) are a series of snapshots taken from the animation of $\lambda_2 = -150$ contour (animation I) from $t = 55.812$ to 55.884 s. These instantaneous snapshots show a typical breakdown process of Görtler vortex. The mechanism can be explained in terms of vortex

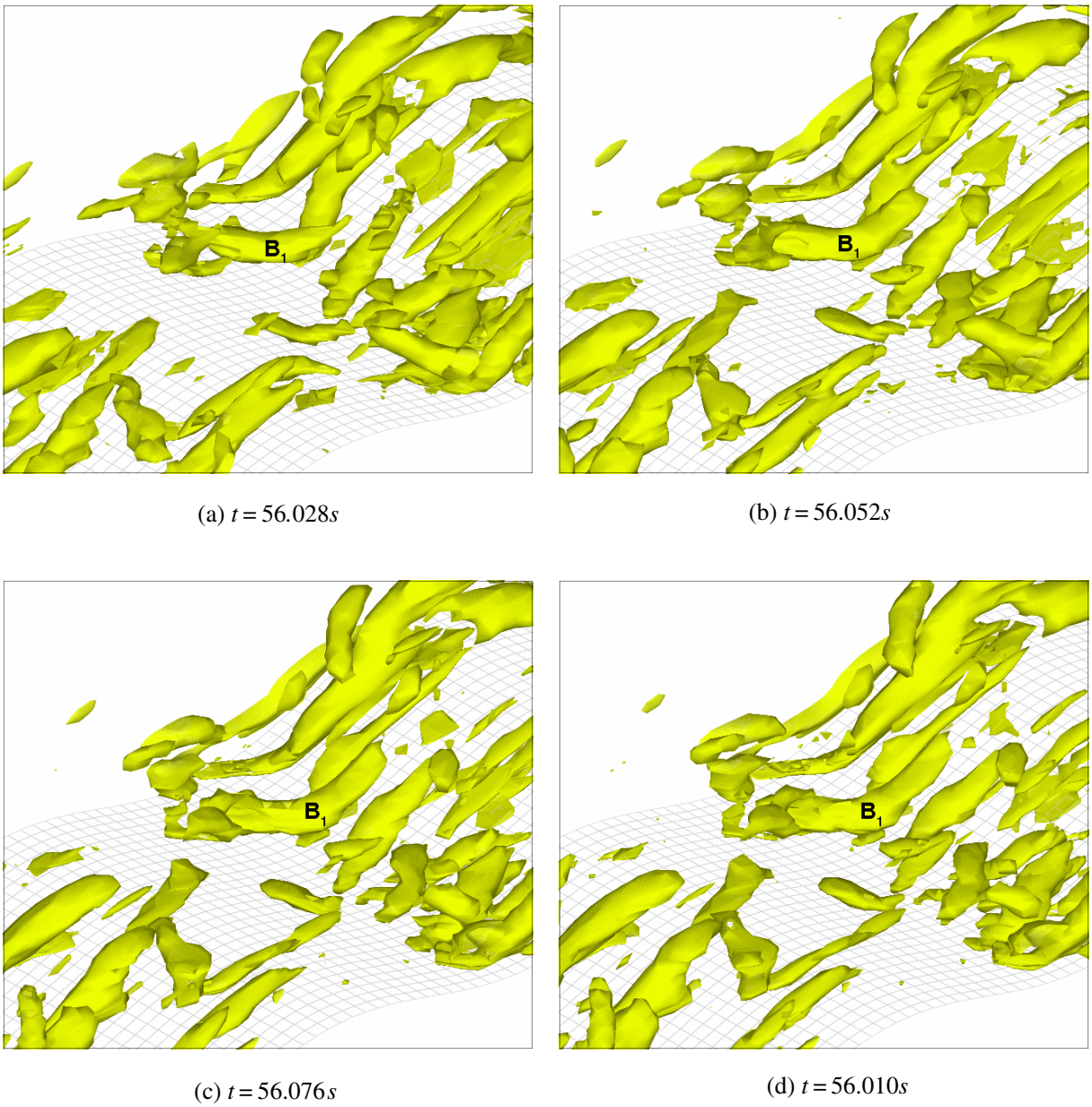

(a) $t = 56.028s$ (b) $t = 56.052s$

(c) $t = 56.076s$ (d) $t = 56.010s$

Figure 11. Time-evolved vortex structures plotted with the λ_2 method in fully developed steady wavy flow (isocontours of $\lambda_2 = -150$).

stretching. Trace the vortex A in figure 12. The vortex A strengthens and elongates on the upslope portion of the wave crest (figure 12(a)). When the vortex A moves further downstream over the wave crest, it loses its identity by further elongation and stretching (figure 12(b)) and then separates into two vortices (vortices A_1 and A_2 in figures 12(c) and (d)). The breakdown process may result from the secondary instability that occurs when the vortex motion begins to saturate. It is also possibly due to the dynamics of the detached shear layer which dominates the momentum tranport in this region. The vortex strength becomes weaker above the convex surface and the streamwise extent of the Görtler vortices is limited. These results are consistent with previous theoretical studies that the convex surface destroys the

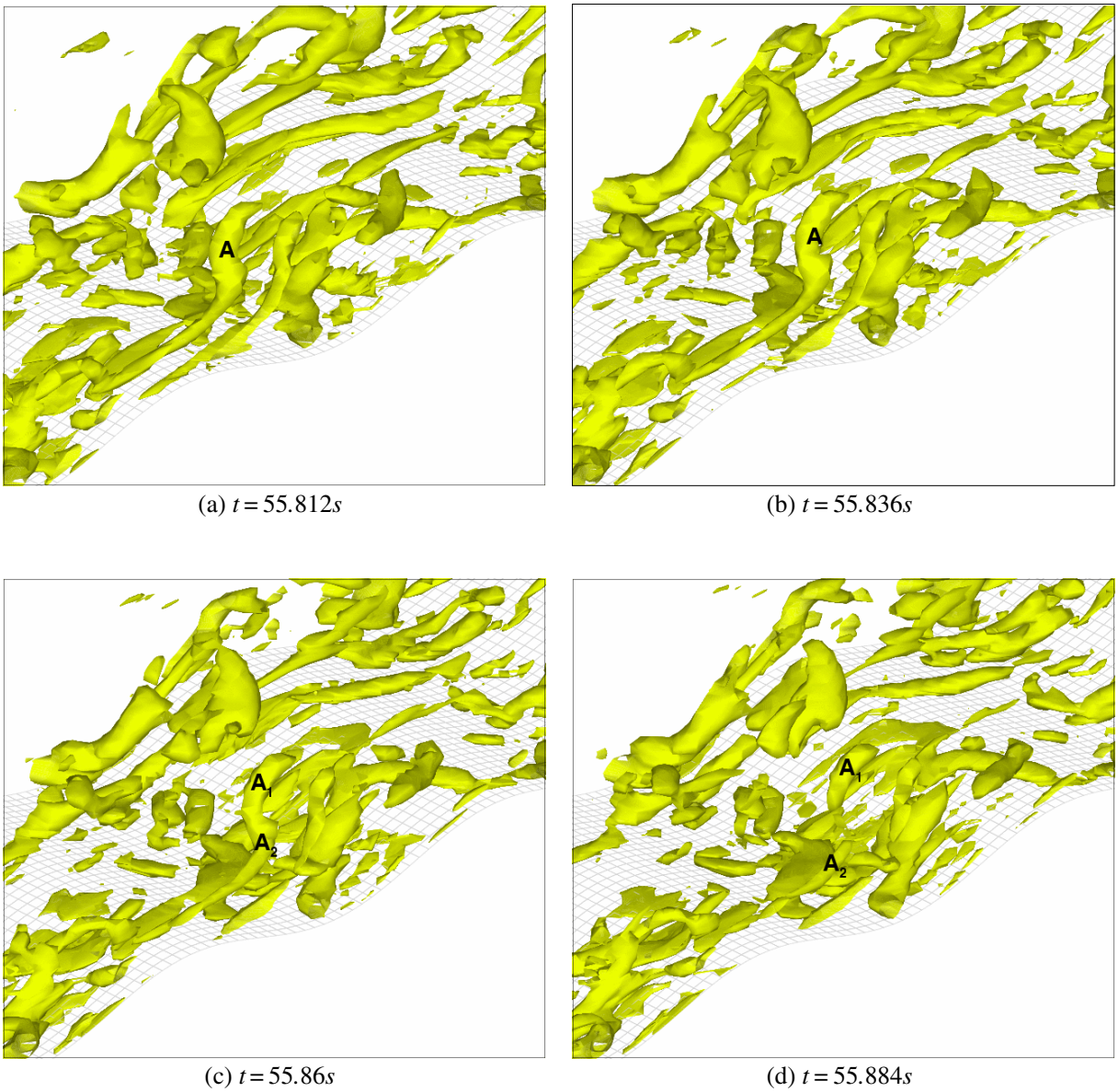

(a) $t = 55.812s$ (b) $t = 55.836s$

(c) $t = 55.86s$ (d) $t = 55.884s$

Figure 12. Time-evolved vortex structures plotted with the λ_2 method in fully developed steady wavy flow (isocontours of $\lambda_2 = -150$). (See animation I.)

vortex through the stabilizing effects. Just downstream of the wave crest, there is a region of negative Görtler number associated with convex boundary curvature which corresponds to the location where the vortices terminate. The location is determined by the geometry (the curvature particularly).

We conclude that the vortex reconnection process leads to the growth of Görtler vortices. When the flow contains perturbations that are three-dimensional, the interactions among the vortices become more complex. These processes appear to be important in fully turbulent wavy boundary flows. In the evolution of Görtler vortices, it is likely that more than one mechanism (instability) is active and play roles in the development and evolution. Note that these processes produce much more complex flow than that explained above. The three-dimensional flow is

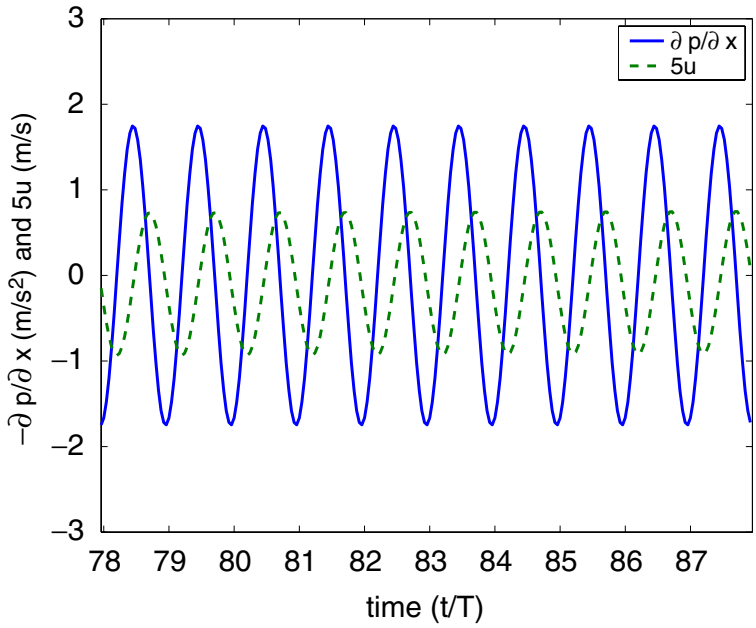

Figure 13. The imposed pressure gradient and the resulting spanwise-averaged streamwise velocity u at the top. Velocity is scaled by a factor of 5.

apparently much more sensitive to small disturbances. Thus the consequence of producing a large amount of Görtler vortices is to increase turbulent mixing and momentum/heat exchange significantly.

3.2. Unsteady flow simulations

We also simulated the unsteady flow over a wavy boundary produced by an oscillatory pressure gradient. As the flow speeds up to its maximum magnitude, it separates at the wave crest, forming a recirculation zone which grows as the flow slows down. The sediment trapped by this spanwise vortex is cast into the outer flow region when the vortex is ejected over the crest during flow reversal. Figure 13 shows the driven pressure gradient $(-\partial p/\partial x)$ and spanwise-averaged velocity u at the top as a function of time. T is the time period imposed by the oscillatory pressure gradient. The time $t = 0$ corresponds to the maximum negative pressure gradient. The spanwise-averaged streamwise velocity (u) in the outer layer has the same form as the driven pressure gradient (a simple sinusoidal function). The flow reaches a balance between the local acceleration and the driving pressure gradient in the outer layer $(\partial u/\partial t = \partial p/\partial x)$ although the influence of topography locally causes accelerations and decelerations near the bottom boundary. The relation between the driven pressure gradient and the spanwise-averaged streamwise velocity at the top can be obtained analytically [15].

Qualitative comparisons between the IBM approach and boundary-fitted grid results of the spanwise-averaged streamwise velocity at two time steps are given in figure 14. Vertical profiles at five locations in one wavelength of the topography are shown. These velocity profiles are phase-averaged over 10 oscillation cycles to obtain stable statistics. Sample taking starts after the flow reaches an oscillatory steady state. The mean profiles show good agreement with boundary-fitted simulations. Some other comparisons can be found in [13].

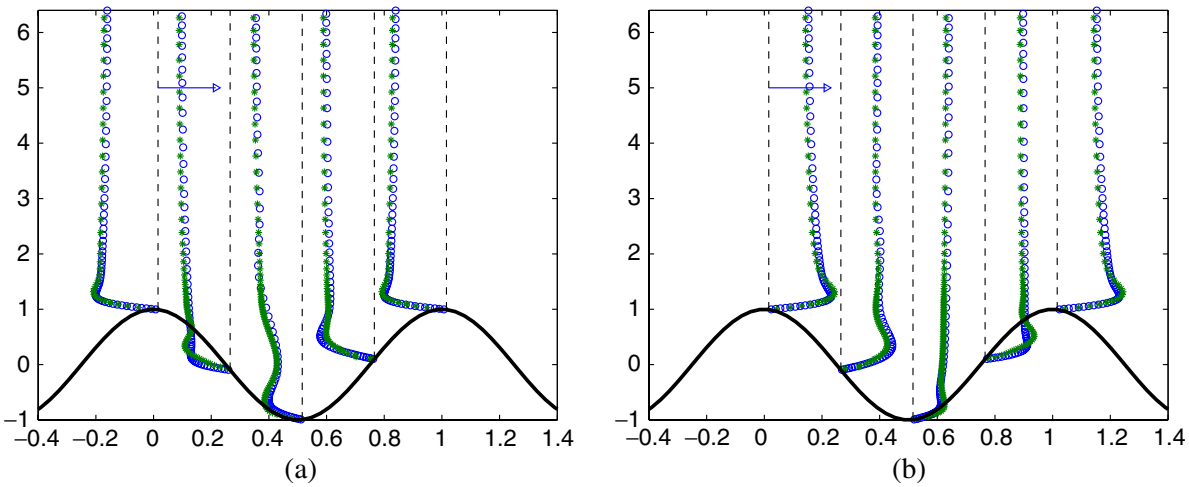

Figure 14. Comparison of streamwise velocity at different time steps: (a) $t/T = 0.5$ and (b) $t/T = 1$. T is the time period imposed by the oscillatory pressure gradient. The arrow at the top denotes 0.0002 $\mathrm{m^2\,s^{-2}}$. ○ , boundary-fitted grid result; and $*$, denotes the IBM result.

The two-dimensional spanwise- and phased-averaged vorticity for an oscillatory cycle are shown in figure 15. The two-dimensional oscillatory flow pattern has been shown to be an efficient mechanism for sediment transport [15]. As shown in figure 13, the flow obtains a balance between the local acceleration and the driving pressure gradient in the outer flow. When the flow speeds up to its maximum magnitude ($t/T = 0.25$) in figure 15, a thin spanwise vortex can be observed in the boundary layer. A small recirculation zone forms just before the pressure gradient has attained its maximum value ($t/T = 0.5$) and the vorticity magnitude reaches its maxima. Recirculation zones appear behind the wave crests but are confined to the few grid points at the bottom. These are similar to vortices obtained with boundary-fitted grids [29].

The boundary layer thickens on the lee side as the recirculation zone grows. The strong upward vertical velocities associated with the recirculation zone cause the structure to grow in vertical extent. As the flow slows down due to the adverse pressure gradient, spanwise vortices form and are lifted off the bottom to roughly the height of the wave crests. The vortex formation/transport process is then repeated as the flow reverses. These results are consistent with the finding of many previous studies [3, 4], in which the development of the spanwise vorticity is very similar and scales with the wave dimension. A more detailed discussion of the sediment transport process subject to these vortex dynamics can be found in [15].

Figure 16 presents the vortex formation/transport process by showing the vortex cores at different time steps from animation II. The formation cycle occurs twice per period, once on either side of a wave trough. From the animation, it can be clearly seen that the cycle starts as the flow accelerates ($t/T = 0.25$) and forms the recirculation zone in the lee side of the crest. The vortex structures are generated by boundary layer separation and the growth of three-dimensional disturbances [36]. They are very thin, some of them extending from just downstream of the crest to the trough in the streamwise direction. These structures are advected downstream as the flow slows down. The boundary layer on the lee side thickens and the recirculation zone is lifted from the bottom. The trends are consistent with the two-dimensional spanwise vorticity description from figure 15 except that the transport is quite variable across the domain. Some of the vortices are centred over the trough. This structure shortens in its streamwise extent

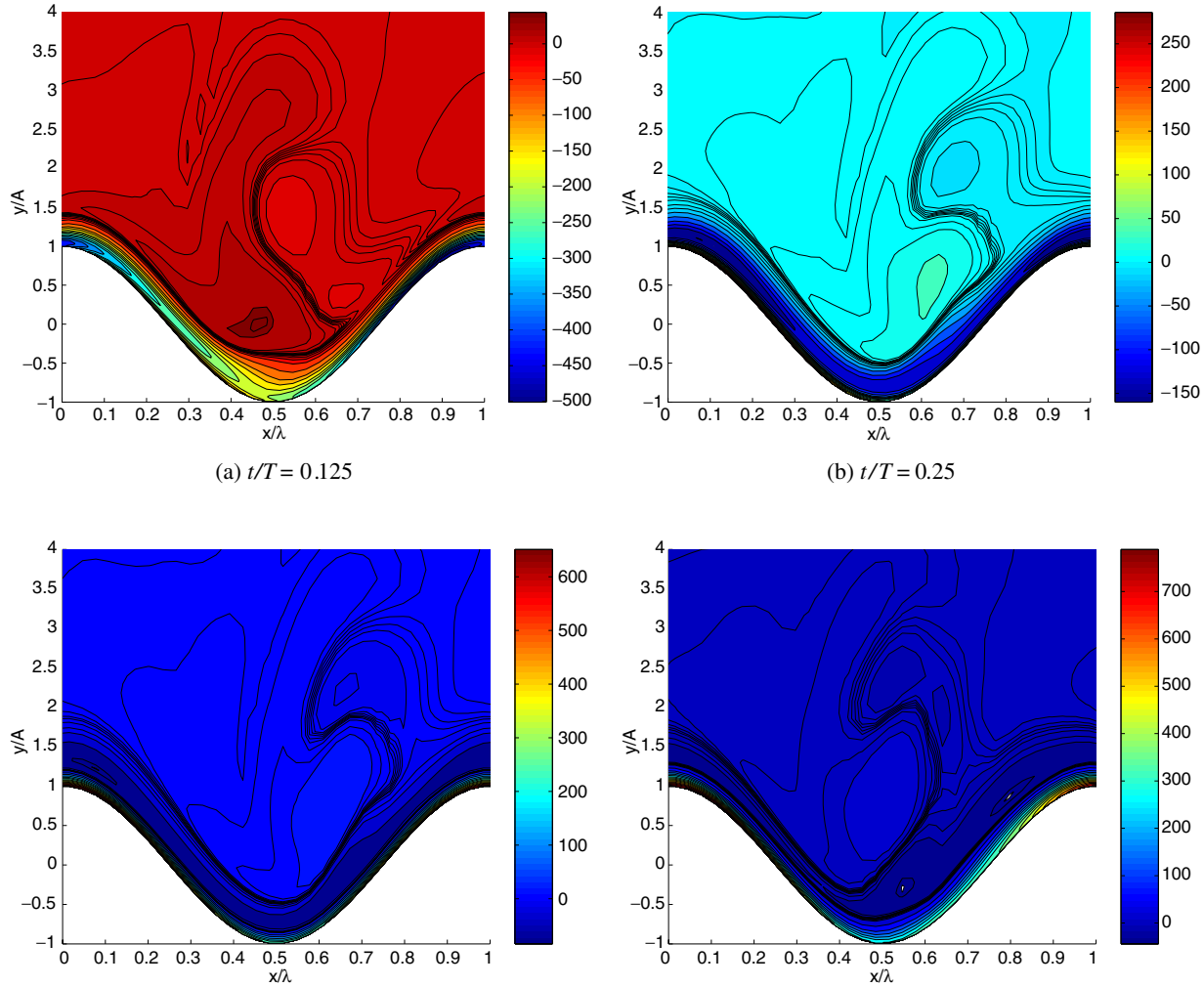

(a) $t/T = 0.125$ (b) $t/T = 0.25$

(c) $t/T = 0.375$ (d) $t/T = 0.5$

Figure 15. The snapshots of two-dimensional spanwise vorticity for an oscillatory cycle. $t/T = 0$, 1 corresponds to the phase of maximum oscillatory pressure gradient.

and breaks up into a more complex, three-dimensional structure as the flow slows further. After the flow switches direction ($t/T = 0.5$), these complex structures are lifted off the bottom and advected over the crest (figure 16). They are stretched in the streamwise direction and lose some of their strength as the flow accelerates in the other direction ($t/T = 0.75$). Then the process repeats in the other direction. The current vortex generation and upward transport mechanism are very similar to those discussed in [36] and the nonlinear effects appear important for the growth of three-dimensional instability.

Figure 17 shows the two dimensional spanwise- and phase-averaged shear stress on the bottom surface at different time steps for an oscillatory cycle. When the flow is approaching its maximum magnitude of streamwise velocity ($t/T = 0.125$, 0.625), the highest shear stress occurs on the upslope portion of the wave crests, and a low shear stress is found in the troughs. The shear-stress distribution is similar to that in figure 9. As the flow accelerates further ($t/T = 0.125-0.25$, $0.625-0.75$), the shear stress decreases and the magnitude of the stress is uniformly

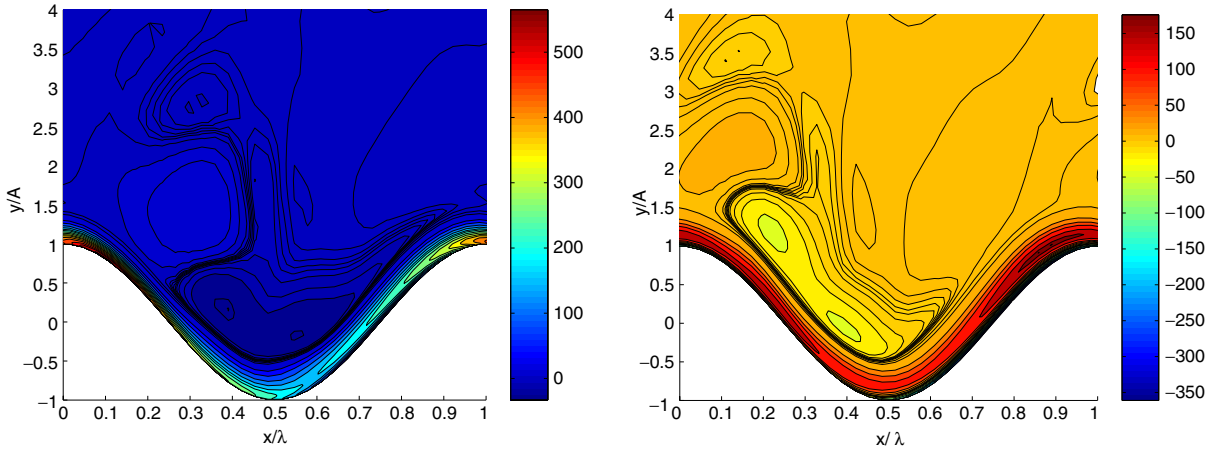

(e) $t/T = 0.625$

(f) $t/T = 0.75$

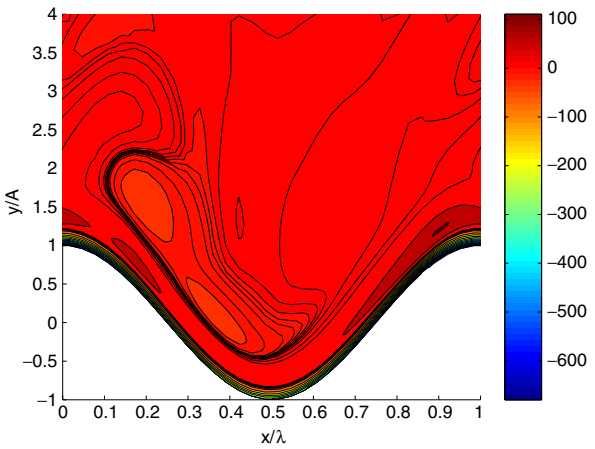

(g) $t/T = 0.875$

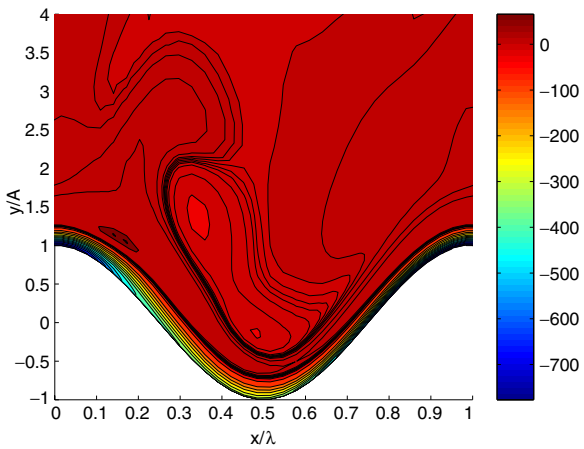

(h) $t/T = 1$

Figure 15. (continued).

small. The shear stress reaches its minima when the velocity has the maximum magnitude ($t/T = 0.25, 0.75$). As the flow slows down towards zero and the recirculation zone intensifies into a coherent spanwise vortex structure, the shear stress in the recirculation zone increases ($t/T = 0.375{-}0.5, 0.875{-}1$). The growth of three-dimensional disturbance also enhances the shear stress on the bottom boundary. When the pressure gradient has attained its maximum value ($t/T = 0.5, 1$), the shear stress magnitude reaches its maxima. It is interesting to note that the maximum shear stress is consistent with the maximum vorticity observed above. The shear stress decreases on the upslopes of wave crests as the flow speeds up again, and the phenomenon is repeated.

4. Conclusions

The aim of this study was to develop an immersed boundary method using second-order ghost-cell reconstruction and demonstrate its applicability in LES. The computation is done on a

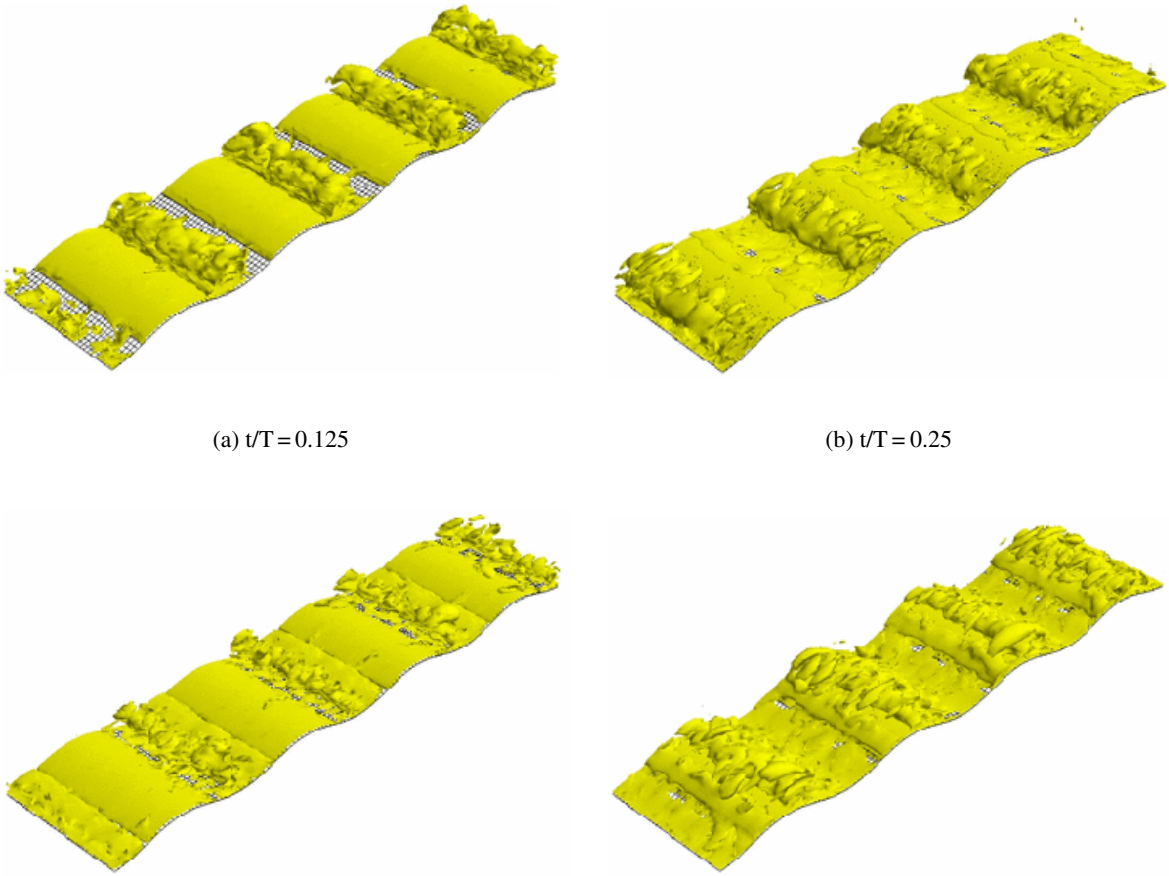

(a) t/T = 0.125 (b) t/T = 0.25

(c) t/T = 0.375 (d) t/T = 0.5

Figure 16. Vortex structures plotted with the λ_2 method for different flow phases during a time period T ($t/T = 0.125$ to $t/T = 1$). $t/T = 0$, 1 corresponds to the phase of maximum oscillatory pressure gradient. The vortices are localized between two contiguous wave crests. (See animation II.)

structured orthogonal mesh. We used the approach to perform LES of three-dimensional turbulent flow over a wavy boundary. Both steady and unsteady flows were simulated and compared with established numerical simulations done on a boundary-fitted grid. The results agree very well with the previous numerical results, indicating the validity and accuracy of the present method. Many vortex structures in flows over a wavy boundary were identified and further investigated in the current study. At high Reynolds numbers, the boundary layer flows over a concave surface develop an alternating sequence of rolling structures under certain conditions. They may angle to the left or right as they move downstream. The animations clearly illustrate the formation/destruction of Görtler vortices in the steady-flow simulation and the three-dimensional vortex formation/transport cycle in the simulation of an unsteady flow. Further investigation is needed to use a more realistic boundary condition (e.g. log-law) for atmospheric applications.

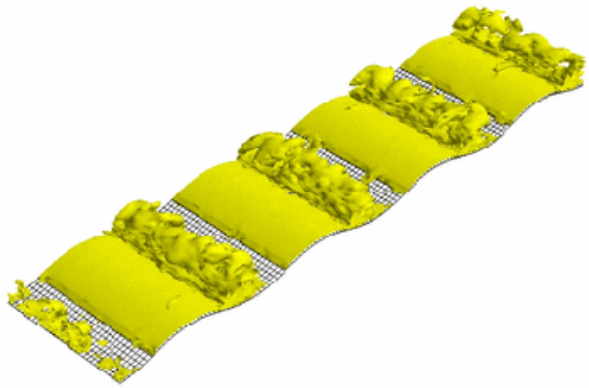

(e) t/T = 0.625

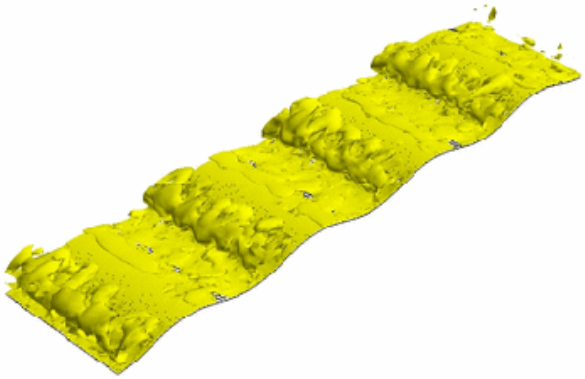

(f) t/T = 75

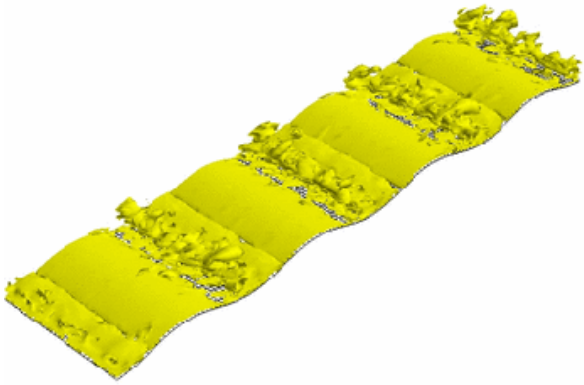

(g) t/T = 1.875

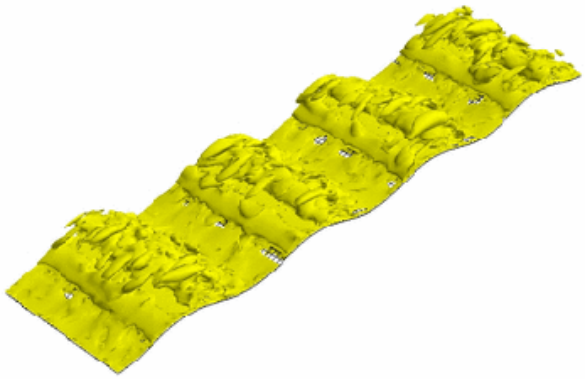

(h) t/T = 1

Figure 16. (continued).

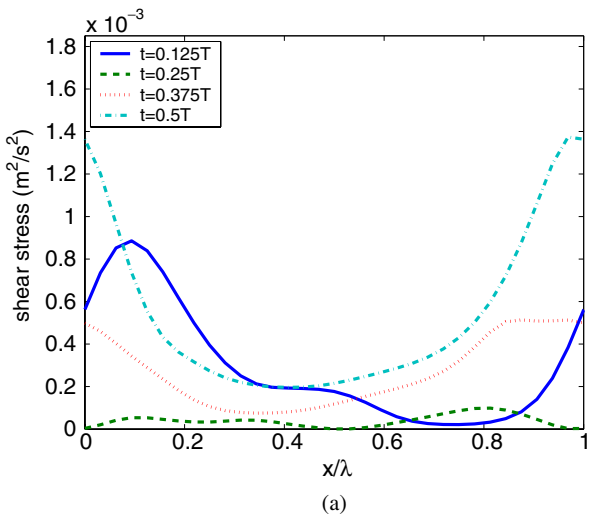

(a)

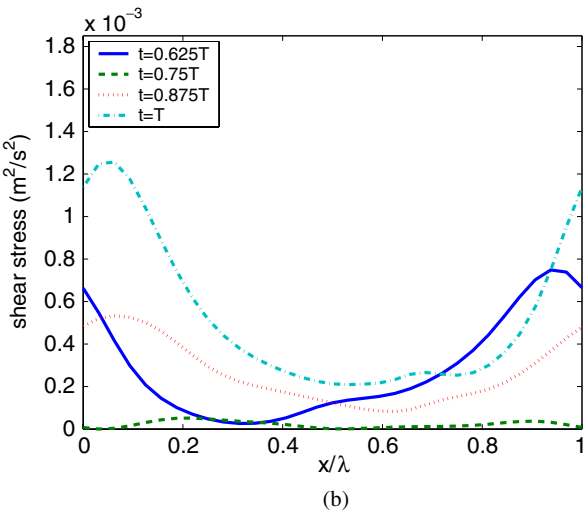

(b)

Figure 17. The magnitude of the bottom shear stress for different flow phases during a time period T ($t/T = 0.125$ to $t/T = 1$). $t/T = 0$, 1 corresponds to the phase of maximum oscillatory pressure gradient.

Acknowledgments

The authors would like to thank Professor R L Street and Dr E Zedler for their invaluable help and continuous support with the turbulent flow simulation and Professor P Durbin and G Iaccarino for useful discussions. Computer time provided at the P A McCuen Environmental Computing Center at Stanford is gratefully acknowledged. Financial support for this work was provided by NSF ITR/AP (GEO) grant number 0113111 and the NASA AMES/Stanford Center for Turbulent Research.

References

[1] Hudson J, Dykhno L and Hanratty T 1996 Turbulent production in flow over wavy wall *Exp. Fluids* **20** 257–65
[2] Buckles J, Hanratty T J and Adrian R J 1984 Turbulent flow over large-amplitude wavy surfaces *J. Fluid Mech.* **140** 27–44
[3] Fredsoe J, Andersen K and Sumer B 1999 Wave plus current over a ripple covered bed *Coastal Eng.* **38** 177–221
[4] Blondeaux P and Vittori G 1991 Vorticity dynamics in an oscillatory flow over a rippled bed *J. Fluid Mech.* **226** 257–89
[5] Calhoun R J and Street R L 2001 Turbulent flow over a wavy surface: neutral case *J. Geophys. Res.* **106** 9277–93
[6] Saric W S 1994 Görtler vortices *Ann. Rev. Fluid Mech.* **26** 379–409
[7] Petitjeans P and Wesfreid J-E 1996 Spatial evolution of Görtler instability in a curved duct of high curvature *AIAA J.* **34** 1793–800
[8] Saric W S and Benmalek A 1991 Görtler vortices with periodic curvature *Boundary Layer Stability and Transition to Turbulence, ASME-FED* vol 114, pp 37–42
[9] Zang Y, Street R L and Koseff J R 1994 A non-staggered grid, fractional step method for time-dependent incompressible Navier–Stokes equations in curvilinear coordinates *J. Comput. Phys.* **114** 18–33
[10] Fadlun E A, Verzicco R, Orlandi P and Mohd-Yusof J 2000 Combined immersed-boundary finite-difference methods for three-dimensional complex flow simulations *J. Comput. Phys.* **161** 30–60
[11] Verzicco R, Mohd-Yusof J, Orlandi P and Haworth D 2000 Large eddy simulation in complex geometry configurations using boundary body forces *AIAA J.* **38** 427–33
[12] Majumdar S, Iaccarino G and Durbin P 2001 RANS solvers with adaptive structured boundary non-conforming grids *Annual Research Briefs* NASA Ames Research Center/Stanford University Center for Turbulence Research, Stanford, CA, pp 353–66
[13] Tseng Y H and Ferziger J H 2003 A ghost-cell immersed boundary method for flow in complex geometry *J. Comput. Phys.* **192** 593–623
[14] Iaccarino G and Verzicco R 2003 Immersed boundary technique for turbulent flow simulations *Appl. Mech. Rev.* **56** 331–47
[15] Zedler E A 2002 Large eddy simulation of sediment transport in oscillatory flow over wavy terrain *PhD Thesis* Stanford University, CA
[16] Osborne P D and Vincent C E 1996 Vertical and horizontal structure in suspended sand concentrations and wave-induced fluxes over bedforms *Marine Geol.* **131** 195–608
[17] Zang Y 1993 On the development of tools for the simulation of geophysical flows *PhD Thesis* Stanford University, CA
[18] Germano M 1992 Turbulence: the filtering approach *J. Fluid Mech.* **238** 325–36
[19] Lilly D K 1992 A proposed modification of the Germano subgrid scale closure method *Phys. Fluids* A **4** 633–35
[20] Kim J and Moin P 1985 Application of a fractional-step method to incompressible Navier–Stokes equations *J. Comput. Phys.* **59** 308–23
[21] Leonard B P 1979 A stable and accurate convective modeling procedure based on quadratic upstream interpolation *Comp. Methods Appl. Mech. Eng.* **19** 58–98
[22] Tseng Y H and Ferziger J H 2001 Effects of coastal geometry and the formation of cyclonic/anti-cyclonic eddies on turbulent mixing in upwelling simulation *J. Turbulence* **2** 014
[23] Peskin C S 1977 Numerical analysis of blood flow in the heart *J. Comput. Phys.* **25** 220–52
[24] Balaras E 2004 Modeling complex boundaries using an external force field on fixed Cartesian grids in large-eddy simulations *Comput. Fluids* **33** 375–404
[25] Saiki E M and Biringen S 1996 Numerical simulation of a cylinder in uniform flow: application of a virtual boundary method *J. Comput. Phys.* **123** 450–65

[26] Goldstein D, Handler R and Sirovich L 1993 Modeling a no-slip flow boundary with an external force field *J. Comput. Phys.* **105** 354–66
[27] Udaykumar H S, Mittal R, Rampunggoon P and Khanna A 2001 A sharp interface Cartesian grid method for simulating flows with complex moving boundaries *J. Comput. Phys.* **174** 345–80
[28] Ye T, Mittal R, Udaykumar H S and Shyy W 1999 An accurate Cartesian grid method for viscous incompressible flows with complex immersed boundaries *J. Comput. Phys.* **156** 209–40
[29] Zedler E A and Street R L 2001 Large-eddy simulation of sediment transport: currents over ripples *J. Hydrau. Eng.* **127** 444–52
[30] Calhoun R J 1998 Numerical investigations of turbulent flow over complex terrain *PhD Thesis* Stanford University, CA
[31] De Angelis V, Lombardi P and Banerjee S 1997 Direct numerical simulation of turbulent flow over a wavy wall *Phys. Fluids* **3** 2429–42
[32] Henn D and Sykes I 1999 Large-eddy simulation of flow over wavy surfaces *J. Fluid Mech.* **383** 75–112
[33] Jeong J and Hussain F 1995 On the identification of a vortex *J. Fluid Mech.* **285** 69–94
[34] Melander M V and Hussain F 1994 Topological vortex dynamics in axisymmetrical viscous flows *J. Fluid Mech.* **260** 57–80
[35] Ferziger J H 1997 Introduction to the physics and simulation of turbulence *Introduction to the Modelling of Turbulence—Lecture Series* von Karman Institute for Fluid Dynamics
[36] Scandura P, Vittori G and Blondeaux P 2000 Three-dimensional oscillatory flow over steep ripples *J. Fluid Mech.* **412** 355–78